JGR Oceans

RESEARCH ARTICLE
10.1029/2021JC017892

Subseasonal-to-Seasonal Forecast Skill in the California Current System and Its Connection to Coastal Kelvin Waves

Dillon J. Amaya[1], Michael G. Jacox[1,2], Juliana Dias[1], Michael A. Alexander[1], Kristopher B. Karnauskas[3,4], James D. Scott[1,3], and Maria Gehne[1,3]

[1]Physical Science Laboratory, Earth System Research Laboratory, National Oceanic and Atmospheric Administration, Boulder, CO, USA, [2]Environmental Research Division, Southwest Fisheries Science Center, National Oceanic and Atmospheric Administration, Monterey, CA, USA, [3]Cooperative Institute for Research in Environmental Sciences, University of Colorado, Boulder, CO, USA, [4]Department of Atmospheric and Oceanic Sciences, University of Colorado Boulder, Boulder, CO, USA

Key Points:

- We have created a new index to describe the time variability of coastally trapped waves over the last 25 years
- The ECMWF S2S forecast model skillfully predicts SSH along the U.S. west coast at leads of up to 4–7 weeks
- Forecast skill is enhanced when the forecast is initialized with strong coastal wave activity

Supporting Information:

Supporting Information may be found in the online version of this article.

Correspondence to:

D. J. Amaya,
dillon.amaya@noaa.gov

Citation:

Amaya, D. J., Jacox, M. G., Dias, J., Alexander, M. A., Karnauskas, K. B., Scott, J. D., & Gehne, M. (2022). Subseasonal-to-seasonal forecast skill in the California Current System and its connection to coastal Kelvin waves. *Journal of Geophysical Research: Oceans*, *127*, e2021JC017892. https://doi.org/10.1029/2021JC017892

Received 12 AUG 2021
Accepted 5 JAN 2022

Author Contributions:

Conceptualization: Dillon J. Amaya, Michael G. Jacox, Juliana Dias, Michael A. Alexander
Data curation: Dillon J. Amaya, Juliana Dias
Formal analysis: Dillon J. Amaya
Funding acquisition: Michael G. Jacox, Juliana Dias, Michael A. Alexander
Investigation: Dillon J. Amaya
Methodology: Dillon J. Amaya, Michael G. Jacox, Juliana Dias, Michael A. Alexander, Kristopher B. Karnauskas, James D. Scott, Maria Gehne
Project Administration: Michael G. Jacox, Juliana Dias, Michael A. Alexander
Resources: Michael G. Jacox

Abstract Accurate dynamical forecasts of ocean variables in the California Current System (CCS) are essential decision support tools for advancing ecosystem-based marine resource management. However, model and dynamical uncertainties present a significant challenge when attempting to incorporate these forecasts into a formal decision-making process. To provide guidance on the reliability of dynamical forecasts, previous studies have suggested that deterministic climate processes associated with atmospheric or oceanic teleconnections may provide opportunities for enhanced forecast skill. Recent computational advances have led to the availability of subseasonal-to-seasonal (S2S) forecasts of key oceanic variables such as sea surface height (SSH), which may be leveraged to identify such "forecast opportunities." In this study, we conduct a S2S forecast skill assessment of SSH anomalies in the CCS using an ensemble of 46-day reforecasts made by the European Center for Medium-range Weather Forecasting (ECMWF) model for the period 2000–2018. We find that the ECMWF model consistently produces skillful dynamical forecasts of SSH, particularly in both the southern and northern CCS at leads of 4–7 weeks. Using a high-resolution ocean reanalysis, we develop a new index designed to characterize the location and intensity of coastally trapped waves propagating through the CCS. We then show that the S2S dynamical forecasts have enhanced skill in forecasts of SSH in weeks 4–7 when initialized with strong or extreme coastally trapped wave conditions, explaining 30–40% more SSH variance than the corresponding persistence forecast.

Plain Language Summary Accurate ocean forecasts along the U.S. west coast are important tools to enable proactive decision making by marine resource managers. However, due to the chaotic nature of the climate system, these forecasts can often be unreliable on timescales of weeks to months. To provide guidance on when such forecasts can be trusted, we analyze the skill of a new ocean forecasting model with a focus on forecasts of sea surface height in the California Current System (CCS) up to 46 days out. We find that the ocean forecasts are skillful, particularly in both the southern and northern CCS at lead times of 4–7 weeks. In addition, we use a high-resolution ocean reanalysis to show that this forecast skill is further enhanced when a particular type of coastal ocean wave is present. Our results provide context for marine resource managers using operational ocean forecasts along the U.S. west coast. We also provide new physical insights into a long-studied ocean process, which opens up innovative and exciting areas for additional analysis.

1. Introduction

Marine stakeholders aiming to proactively manage sensitive fisheries and marine ecosystems along the U.S. west coast may benefit from accurate forecasts of coastal ocean conditions in the California Current System (CCS). In particular, wildlife managers seek decision support tools to help prepare for ecosystem impacts associated with natural and anthropogenically forced climate variability and change (Jacox et al., 2020; Tommasi et al., 2017). As a result, there has been increased emphasis in recent years on the development (e.g., Kirtman et al., 2014; Vitart et al., 2017) and evaluation (e.g., Hervieux et al., 2019; Jacox et al., 2020; Shin & Newman, 2021; Siedlecki et al., 2016; Stock et al., 2015) of climate forecasting models for marine ecosystem applications.

Climate forcing modulates oceanic variables throughout the CCS on a continuum of timescales (from days to decades); however, there has been a particular focus on assessing and improving seasonal-to-interannual (S2i;

Software: Dillon J. Amaya, Juliana Dias
Supervision: Michael G. Jacox, Juliana Dias, Michael A. Alexander, Kristopher B. Karnauskas
Validation: Dillon J. Amaya, Juliana Dias, Kristopher B. Karnauskas
Visualization: Dillon J. Amaya, Juliana Dias, Kristopher B. Karnauskas, James D. Scott
Writing – original draft: Dillon J. Amaya
Writing – review & editing: Dillon J. Amaya, Michael G. Jacox, Juliana Dias, Michael A. Alexander, Kristopher B. Karnauskas, James D. Scott, Maria Gehne

1–24 months) forecast skill (e.g., Jacox et al., 2020). While S2i is indeed a significant time horizon for marine ecosystem management decisions (Hobday et al., 2018), subseasonal-to-seasonal (S2S; 1–60 days) timescales also represent an important forecasting window for decision making. For example, short-term (e.g., days to weeks) predictions of nearshore sea level are important for improving infrastructure resilience to coastal inundation (DeMott et al., 2021; Nichols et al., 2019; Woodworth et al., 2019), and sea level is one of a suite of variables (also including temperature, currents, and others) that can be used as predictors of fisheries bycatch and ship-strike risks in the CCS (Hazen et al., 2017, 2018; Howell et al., 2008; Thorne et al., 2019; Welch et al., 2019).

In the past several decades, there has been a concerted effort to assess S2S forecasting skill of atmospheric variables such as precipitation and near-surface air temperature (e.g., Vitart et al., 2017; Vitart & Robertson, 2018); however, there has been considerably less research evaluating S2S forecasts of marine resource-relevant oceanic variables. This discrepancy may in part be due to the slow evolution of the ocean compared to the atmosphere (e.g., Goddard et al., 2001), which could result in damped persistence as the best forecast of ocean variables on S2S timescales. Indeed, if that were the case, then there would be little utility for a dynamical ocean forecast at lead times of days to several weeks. However, there are a number of large-scale climate interactions that may provide so-called "forecast opportunities" (Stan et al., 2017), in which the forecast skill at a particular place is enhanced on S2S timescales due to the deterministic evolution of the climate system. For example, atmospheric teleconnections related to the El Niño-Southern Oscillation (ENSO), the Madden-Julian Oscillation (MJO), and other phenomena (Capotondi et al., 2019) may represent one such forecast opportunity. In the span of 2–3 weeks, an atmospheric Rossby wave train generated by anomalous tropical convection can alter the surface wind field near the U.S. west coast (Seo & Son, 2012; Simmons et al., 1983; Wallace & Gutzler, 1981) and lead to rapid shifts in the regional distribution of key ocean parameters, such as sea surface temperature (SST) and sea surface height (SSH). As a result, knowledge of the current ENSO or MJO phase at initialization may provide an indication of whether subsequent forecasts of oceanic variables in the CCS will be skillful at various lead times (Jacox et al., 2019).

Another potential S2S forecast opportunity may be related to oceanic teleconnections in the form of rapidly propagating ocean Kelvin waves (KW). These first-mode baroclinic KWs are typically forced in the western equatorial Pacific by the acceleration of anomalous near equatorial surface winds associated with intraseasonal atmospheric phenomena, such as the MJO, the monsoon, and extratropical intrusions (Hendon et al., 1998; Kessler et al., 1995; Luther et al., 1983; Seiki & Takayabu, 2007; Zhang, 2001). In particular, westerly wind anomalies in the western equatorial Pacific drive anomalous downwelling, a depressed thermocline, and increased SSHs (Kutsuwada & McPhaden, 2002). The opposite is true for easterly surface wind anomalies.

Once formed, the thermocline and SSH signature of the KWs will propagate eastward with an average phase speed of ∼2.7 m/s, crossing the equatorial Pacific in ∼50–70 days (Busalacchi et al., 1983; Cravatte et al., 2003; Eriksen et al., 1983; Roundy & Kiladis, 2007; Rydbeck et al., 2019; Shinoda et al., 2008). Due to their role in modulating the eastern equatorial Pacific thermocline, intraseasonal KWs play a critical role in the development and intensification of ENSO events (e.g., Batstone & Hendon, 2005; Bergman et al., 2001; Karnauskas, 2013; Kessler & Kleeman, 2000; Kessler & McPhaden, 1995; McPhaden, 1992, 1999; McPhaden et al., 1988; McPhaden & Yu, 1999; Mosquera-Vásquez et al., 2014; Seo & Xue, 2005).

Upon reaching the South American coastline, KWs can continue propagating poleward as coastally trapped waves (CTWs) along the west coast of the Americas (Enfield & Allen, 1980; Enfield et al., 1987). Despite the meandering geometry of the coastline and the highly varying bathymetry of the coastal waters, observational and modeling studies have detected the wave energy associated with these CTWs well into the CCS and as far north as the Gulf of Alaska several months after leaving the equator (Frischknecht et al., 2015; Gómez-Valdivia et al., 2017; Johnson & O'Brien, 1990; Lyman & Johnson, 2008). However, during their poleward travel, the characteristics and the phase speeds of these waves may differ from their tropical origins, as they can evolve into hybrids of topographic and baroclinic shelf waves (e.g., Enfield & Allen, 1983). This is further complicated by the local generation of CTWs along the coast by random wind forcing or by sloped bottom boundaries (Frischknecht et al., 2015; Hughes et al., 2019; Wang & Mooers, 1976)

Coastally trapped KWs have a narrow horizontal footprint, extending ∼100 km offshore in the tropics and narrowing to ∼20 km at high latitudes. However, as they propagate, they strongly modify the vertical water column structure, which alters ocean parameters such as SSH, SST, and bottom temperature and can impact sensitive

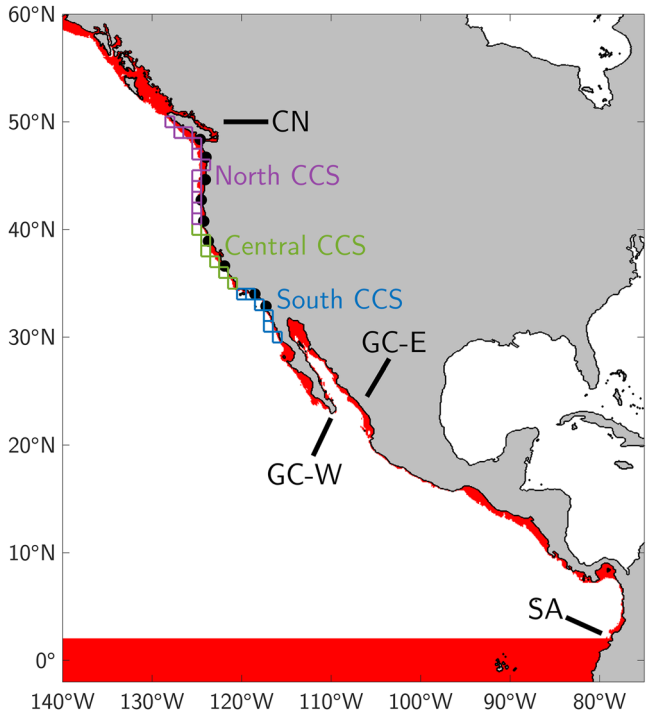

Figure 1. Kelvin wave propagation pathway on the GLORYS grid. Red shading along equator indicates 2°S–2°N. The equatorial pathway extends westward beyond the figure bounds to 150°E. Red shading along coast marks GLORYS 1/12° × 1/12° grid cells with bottom depths shallower than 400 m. Colored boxes denote coastal S2S model 1° × 1° grid cells. Box color corresponds to the respective California Current System (CCS) regional averages. Black dots mark the locations of the nine tide gauges used to verify GLORYS monthly mean SSH (see also Figure 2). Black text and lines denote geographical waypoints along the Kelvin wave pathway.

marine ecosystems found along the shallow continental shelf (e.g., Ding et al., 2021; Jacox et al., 2018). Additionally, elevated sea level driven by coastal KWs can lead to coastal inundation, threatening coastal infrastructure and endangering people (Jacox et al., 2020; Widlansky et al., 2017; Woodworth et al., 2019).

Given the influence of CTWs on U.S. west coast sea level, and potentially on marine ecosystems more broadly, it would be beneficial to determine whether these waves act as a forecast opportunity and contribute to enhanced forecast skill of coastal ocean variables on S2S timescales. In this study, we use a combination of in situ measurements and a high-resolution ocean reanalysis to identify intraseasonal ocean waves propagating from the western equatorial Pacific to the Gulf of Alaska. In particular, we introduce an intensity index that describes the time variability of CTWs that have traveled along the U.S. west coast over the past 25 years. We then use these novel observational tools to conduct the first S2S skill assessment of coastal CCS SSH using a state-of-the-art forecast model. Our focus on coastal SSH is an important first step in validating the physical evolution of the S2S ocean forecasts since SSH is dynamically linked to many other impactful oceanic variables through its influence on thermocline depth, upwelling rates, and horizontal current velocities (Jacox et al., 2015). We find that dynamical forecasts of SSH in the CCS are significantly more skillful than persistence at leads of up to 7 weeks. We further show that this forecast skill increases when the forecast is initialized with a strongly propagating CTW signature.

2. Data and Methods

2.1. High-Resolution Ocean Reanalysis

To characterize intraseasonal ocean wave variability in the historical record, we use the GLORYS ocean reanalysis version 12v1 (Lellouche et al., 2021). Generated by the Copernicus Marine Environmental Monitoring Service (CMEMS), GLORYS offers daily mean and monthly mean ocean variables at 1/12° horizontal resolution with 50 vertical levels. The reanalysis is generated using the Nucleus for European Modeling of the Ocean (NEMO) ocean model, forced at the surface by the European Center for Medium-Range Weather Forecasts (ECMWF) ERA-Interim atmospheric reanalysis. Data are available from 1993 to 2018, during which the model assimilates along-track satellite altimetry, satellite SST, sea ice concentrations, and in situ profiles of temperature and salinity from the Coriolis Ocean database ReAnalysis (CORA) data set (Szekely et al., 2019). Unless otherwise specified, we analyze daily mean GLORYS SSH anomalies, which are relative to an unsmoothed long-term daily mean climatology from 2000 to 2018.

Its high spatial and temporal resolution make GLORYS an ideal tool to characterize the fine-scale structure of intraseasonal CTWs as they propagate through the CCS. However, even with 1/12° horizontal resolution, small-scale yet potentially important coastal features may not be well resolved. Additionally, satellite altimetry has known errors on small scales near coastlines (Vignudelli et al., 2019), suggesting that GLORYS may be more reliant on the underlying ocean model in these regions. Therefore, in order to gain confidence in GLORYS ability to accurately simulate coastal SSH variability, we first verify GLORYS output using in situ measurements of sea level from nine tide gauges found along the U.S. west coast (Figure 1, black dots). The tide gauges are not assimilated into GLORYS, and therefore offer an independent metric by which to verify the reanalysis. At every station, the nearest GLORYS grid cell does an excellent job of capturing the monthly mean and daily mean sea level variability measured by the tide gauge, with anomaly correlation coefficients ranging from 0.84 in the Pacific Northwest to 0.9 in Southern California for monthly means and 0.74 to 0.84 for daily means (Figure 2 and Table 1). As a result, we can use GLORYS to assess the S2S forecast model. See Supporting Information for more details on the tide gauge comparisons.

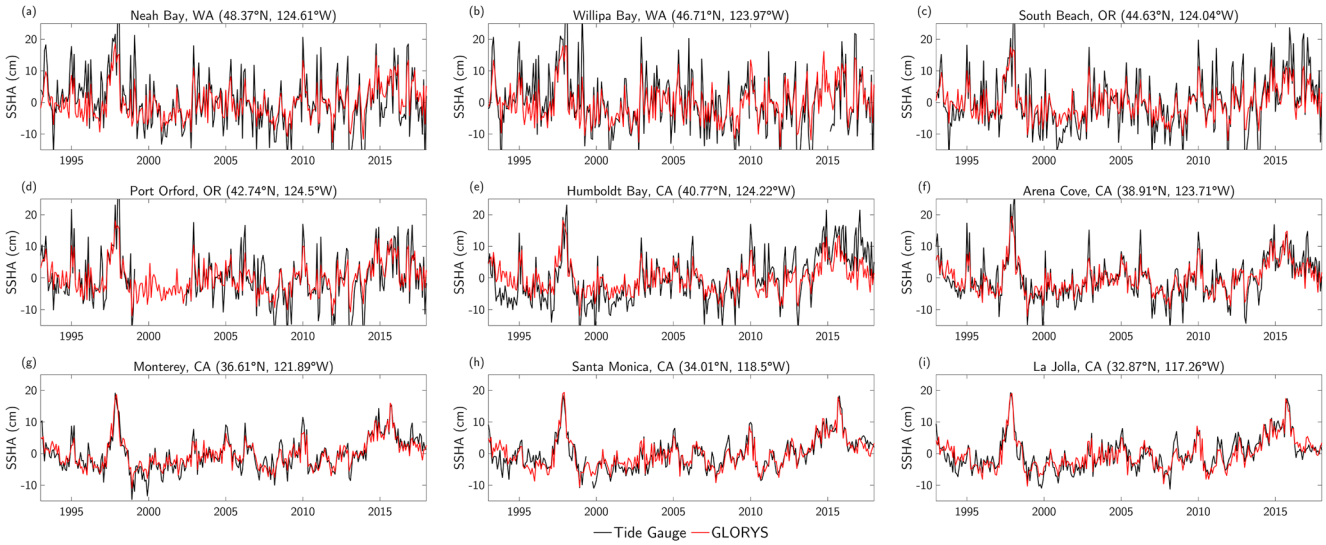

Figure 2. Monthly mean sea surface height (SSH) anomalies (cm) from nine tide gauge stations along the U.S. west coast (black) and the nearest GLORYS grid cells (red). Tide gauge locations are in the subpanel titles and are marked by black dots in main text Figure 1. Correlations and root-mean-square error (RMSE) values between the GLORYS and tide gauge data at each station are in Table 1.

2.2. S2S Reforecasts

Reforecasts of SSH are obtained from the S2S weather prediction database hosted by ECMWF. While this database archives output from 11 S2S forecasting models, currently ECMWF is one of only three modeling centers that makes SSH reforecasts publicly available. Here we use the ECMWF model version CY46R1. The ocean model is NEMO3.4.1, which is run at 0.25° horizontal resolution with 75 vertical levels, although the ocean variables are only available at 1° resolution for analysis. Reforecasts for 46 days are initialized every 3–4 days beginning January 2, 2000. Each reforecast consists of 11 total ensemble members, which include: (1) A single control forecast, initialized at day 0 with data from the ERA5 atmospheric reanalysis and the Ocean Reanalysis System 5 (ORAS5), and (2) A set of 10 perturbation forecasts that have slightly altered initial conditions.

Table 1
Correlation and Root-Mean-Square Error (RMSE; cm) Values Between Sea Level Anomalies Taken at Nine Tide Gauges Along the US West Coast (Figure 1; Black Dots) and Those From the Nearest Grid Cell in the GLORYS Ocean Reanalysis

	Monthly mean		Daily mean	
Tide gauge	Correlation (R)	RMSE (cm)	Correlation (R)	RMSE (cm)
Neah Bay, WA	0.84	5.04	0.81	9.37
Willipa, WA	0.85	5.27	0.84	10.74
South Beach, OR	0.88	4.54	0.82	8.59
Port Orford, OR	0.86	4.44	0.81	8.04
Humboldt Bay, CA	0.84	4.53	0.74	7.92
Arena Cove, CA	0.88	3.17	0.75	6.86
Monterey, CA	0.91	2.23	0.78	4.70
Santa Monica, CA	0.90	2.22	0.79	4.03
La Jolla, CA	0.90	2.28	0.78	4.20

Note. Statistics are separated for monthly mean and daily mean values. All correlations are significant at 95% confidence using a Student's t test. See Figure 2 for monthly mean time series and precise tide gauge coordinates.

Unless otherwise stated, comparisons between the ECMWF SSH reforecasts and GLORYS are for the period January 2, 2000 to November 16, 2018, which includes a total of 1,982 forecasts. Since the model will drift toward its preferred (biased) state over the course of a forecast, we calculate SSH anomalies relative to a lead-dependent climatology from 2000 to 2018. Skill evaluation is based on the squared anomaly correlation coefficient (R^2) between the ensemble mean S2S SSH anomalies and GLORYs SSH anomalies as a function of lead time and initialization day. We also calculate the root-mean-square error (RMSE) between the S2S anomaly forecasts and the GLORYS SSH anomalies (see Hervieux et al., 2019, Equations 1 and 2 for more details).

In order to capture the distinct biological and physical regimes found along the U.S. west coast (Checkley & Barth, 2009; Dorman & Winanat, 1995; Jacox et al., 2019), we evaluate forecast skill separately for the Southern, Central, and Northern CCS, which is divided at Pt Conception (~34.5°N) and Cape Mendocino (~40.5°N) and is illustrated by blue, green, and purple grid boxes in Figure 1. When comparing to the S2S data, GLORYS daily mean SSH anomalies were averaged separately in these same 1° × 1° boxes. The GLORYS data in each region were then subsampled in time to match the

initialization and forecast dimensions of the S2S data. All comparisons between the S2S model and GLORYS are with unfiltered SSH anomalies.

The S2S forecast skill is further compared against damped persistence, which assumes that SSH anomalies decay toward zero over some characteristic timescale. Due to the slow evolution of the ocean (e.g., Goddard et al., 2001), damped persistence is often a skillful forecast for many oceanic variables. Additional skill above persistence indicates the added value of a dynamical forecast system. The damped persistence forecast at a given location x and lead t is equal to the GLORYS SSH anomaly at initialization multiplied by the SSH autocorrelation function at location x and lag t. Forecast skill significance was determined following Stock et al. (2015), which uses a Fisher's Z transformation (Fisher, 1915, 1924; Lund et al., 2000) to determine whether the dynamical forecast R^2 is: (a) Significantly above 0, and (b) Significantly greater than the persistence forecast R^2. For our comparisons, we use a 90% confidence interval to denote significance. See Stock et al. (2015) for more details.

2.3. Kelvin Wave Hovmöller Pathway

In order to capture the full lifecycle of an ocean KW—from an equatorially trapped disturbance originating in the western Pacific all the way to a CTW in the Gulf of Alaska—we reduce the GLORYS SSH data from 3D (i.e., time × latitude × longitude) into 2D (time × space; i.e., a Hovmöller), where the new spatial dimension traces the ∼30,000 km pathway followed by a typical propagating KW (Figure 1; red shading). Starting in the western equatorial Pacific at 150°E, the pathway runs eastward to the South American coast in the eastern equatorial Pacific (SA; Figure 1). From there, the pathway's positive direction follows the Central American coastline going northward, ultimately entering the Gulf of California on the eastern side (GC-E; Figure 1) before tracing the inner coastline of the Sea of Cortés, flowing southward, and exiting the Gulf of California on the western side (GC-W; Figure 1). The pathway then wraps around the Baja California Peninsula, continuing northward along the U.S. west coast to Canadian waters (CN; Figure 1). A KW traveling at typical phase speeds of ∼2.7 m/s (e.g., Roundy & Kiladis, 2007; Shinoda et al., 2008; Strub & James, 2002) would transit the full pathway in ∼120 days.

To map the GLORYS SSH data onto this pathway, we meridionally average SSHs from 2°S-2°N along the equatorial leg from 150°E to SA (Figure 1; equatorial red shading). We then only consider grid cells along the Central and North American coastlines with bottom depths shallower than 400m (Figure 1; coastal red shading) and zonally average SSH at each latitude, such that at every latitude along the coast we have an approximation of the nearshore SSH. We then concatenate the coastal zonal averages in the along-path direction to create our one-dimensional space following the pathway. Along-path anomalies are then plotted against the total distance traveled (in km) moving from the western equatorial Pacific to the Gulf of Alaska. Care was taken near the Gulf of California to only zonally average grid cells associated with the current location along the path (e.g., we did not zonally average all grid cells at the same latitude across Baja California and the Gulf of California, where the path crosses the same latitude three times).

2.4. Wavenumber-Frequency Spectral Analysis

To assess the S2S model's ability to accurately simulate ocean KWs, we compare the wavenumber-frequency spectra of equatorial SSH anomalies between GLORYS and the S2S model at different leads (see Section 3.4). In each case, the spectrum is calculated using unfiltered SSH anomalies averaged 2°S–2°N from 170°W to the South American coastline. This results in matrices with dimensions $M \times N$ where M is space and N is time. For GLORYS, the time dimension includes continuous daily mean data from January 1, 2000 to December 31, 2018 ($N = 6{,}935$, ignoring leap days) and the spatial dimension is on the GLORYS 1/12° grid ($M = 1{,}098$). For the S2S model, in order to create a continuous time series for analysis we linearly interpolate the S2S forecasts (initialized every 3–4 days) to daily resolution. This results in an estimated 46-day forecast every day from January 2, 2000 to November 16, 2018 ($N = 6{,}889$, ignoring leap days). The S2S forecast spatial dimension is on the 1° ECMWF grid ($M = 90$).

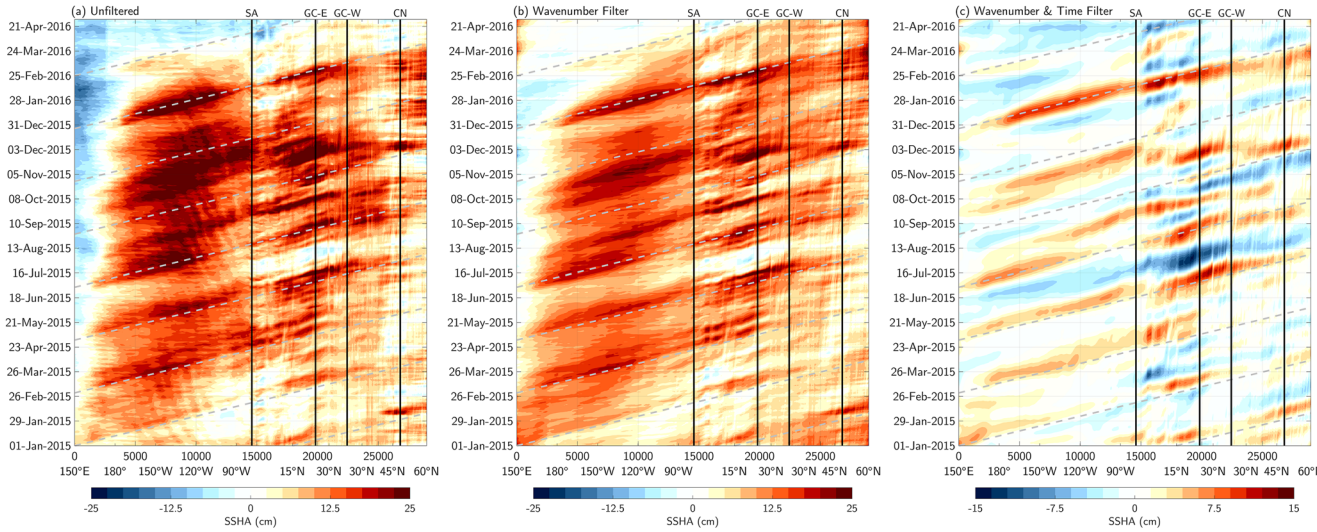

Figure 3. (a) Unfiltered, (b) wavenumber filtered, and (c) wavenumber and time filtered sea surface height (SSH) anomalies (cm) along the Kelvin wave pathway from January 1, 2015 to April 30, 2016. Vertical black lines correspond to geographical waypoints indicated in Figure 1. Dashed gray lines indicate a phase speed of 2.7 m/s. Upper *x* axis marks the distance along the pathway in kilometers. Lower *x* axis marks the approximate latitude/longitude coordinates at select locations along the path.

3. Results

3.1. Sample Kelvin Waves in the GLORYS High-Resolution Ocean Reanalysis

To illustrate propagating intraseasonal KWs waves in the GLORYS high-resolution ocean reanalysis, we show Hovmöller diagrams of daily mean SSH anomalies along the KW pathway from January 1, 2015 to April 30, 2016 (Figure 3). This time period is of particular interest to the marine ecosystem impacts community due to the development of the extreme 2015/2016 El Niño event, which contributed to the evolution and persistence of extremely warm ocean temperatures along the U.S. west coast related to the 2013–2016 Northeast Pacific marine heatwave (Amaya et al., 2016; Bond et al., 2015; Jacox et al., 2016).

Using unfiltered GLORYS data (Figure 3a), we see elevated SSH anomalies throughout this time period. However, embedded in the large-scale feature are bands of SSH anomalies propagating in the positive along-path direction. These banded structures originate in the western equatorial Pacific and propagate eastward toward the South American coast (marked by the vertical black line labeled "SA"). Propagating positive SSH anomalies are consistent with downwelling KWs, which grow in amplitude with each successive wave as the 2015/2016 El Niño matures through boreal winter.

Upon reaching the South American coastline, the downwelling KWs appear to transition into CTWs along the Central and North American coastlines (i.e., between SA and CN). However, there is also a great deal of noise in the SSH anomaly field that is unrelated to downwelling KW propagation, making it difficult to isolate each discrete wave as it passes a particular location. This noise may be due to local wind forcing generated by stochastic weather or by remote teleconnections associated with the developing El Niño (i.e., the atmospheric bridge). To more clearly identify the KWs as they propagate along the path, we first apply a wavenumber filter which retains only positive wavenumbers (i.e., waves traveling in the positive along-path direction; Figure 3b). We then bandpass filter the data using a 20–180 days Lanczos filter to isolate intraseasonal variability (Figure 3c). With both the wavenumber and time filtering applied, the individual KWs are readily apparent as coherent bands of propagating positive or negative (in the case of upwelling KWs) SSH anomalies.

The KWs during this period have diverse life cycles. For example, the downwelling KW beginning in early March 2015 originates in the western equatorial Pacific and transits the width of the equatorial Pacific in ~70 days, but the wave energy dissipates up the Central American coastline before reaching the Gulf of California. In contrast, there are CTWs that strongly project up the coastline, but are only weakly linked to prior equatorial anomalies. These features may be related to CTWs generated by local wind forcing, independent of preceding equatorial wave conditions (Enfield & Allen, 1983; Frischknecht et al., 2015). Finally, there are a number of downwelling

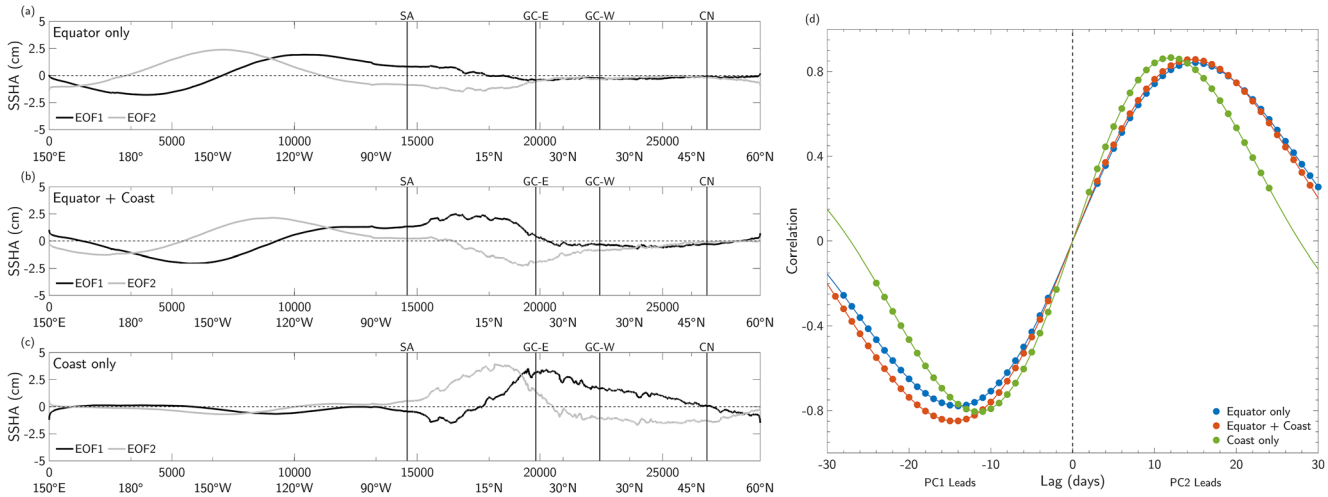

Figure 4. The first two empirical orthogonal functions (EOFs) of filtered sea surface height (SSH) anomalies (cm) in the (a) Equator only, (b) Equator + Coast, and (3) Coast only domains. The *x* axis notation and vertical black bars are the same as in Figure 3. (d) Lag correlations between each PC1 and PC2 pair. Stippling denotes significant correlations at a 90% confidence interval.

KWs (and one upwelling KW beginning in mid-June 2015) that clearly transit the full ∼30,000 km pathway, from the western equatorial Pacific to the eastern equatorial Pacific (in ∼60–70 days) and then northward up the coastline to the Gulf of Alaska (in ∼50–60 days; Figure 3c).

The diversity of KWs and CTWs during this time period highlights the need to consider various dynamical drivers, both remote (e.g., from the tropics) and local (e.g., along the coast), that may excite intraseasonal coastal waves capable of impacting the CCS. We will discuss this topic in more detail in Section 3.3. Regardless of flavor, however, each wave propagates at a phase speed of ∼2.7 m/s (Figure 3; dashed gray lines), even those that transit complicated coastlines and bathymetric structures such as the inner coastline of the Gulf of California (i.e., GC-E to GC-W). There is, however, evidence of a slight phase speed increase as the CTWs wrap around Baja California and make their way along the U.S. west coast (i.e., GC-W to CN).

3.2. Kelvin Wave EOF Patterns

Before evaluating the S2S reforecasts and determining whether CTWs inherently improve forecast skill, we must quantify the overall time variability of KWs as they travel along the equator and potentially through the CCS. Doing so allows us to stratify the S2S forecasts based on the presence (or lack) of CTWs at forecast initialization. As a first step, we characterize intraseasonal KWs propagating along the equatorial Pacific following the methods of Rydbeck et al. (2019). In short, this method involves computing empirical orthogonal functions (EOFs) of GLORYS SSH anomalies along the equatorial portion of the KW path (i.e., 2°S–2°N averaged from 150°E until the South American coastline; referred to as "Equator only"). The SSH anomalies for this procedure were calculated by removing the first three harmonics of the seasonal cycle from the data. Prior to the EOF calculation, the SSH anomalies were wavenumber filtered to only retain positive wavenumbers (i.e., waves propagating in the positive along-path direction) and then bandpass filtered in time using a 20–180 days Lanczos filter (as in Figure 3c).

To illustrate the relevant EOF spatial patterns, we regress filtered SSH anomalies along the KW pathway onto the corresponding principal components (PCs; Figure 4a). Results are similar if we instead regress unfiltered data. The first two Equator only EOFs explain 39.8% and 35.3% of the SSH variability, respectively. The first EOF is characterized by a SSH dipole, with negative anomalies in the western equatorial Pacific and positive anomalies in the eastern equatorial Pacific. The second EOF pattern is dominated by large positive SSH anomalies in the central equatorial Pacific. Each EOF only weakly projects on the Central American coastline (i.e., between SA and GC-E). The corresponding PC1 and PC2 are phase lagged with a correlation of −0.78 when PC1 leads by 14 days (Figure 4d; blue line). This indicates that, when combined, EOF1 and EOF2 represent a wave that propagates SSH anomalies from west to east along the equatorial Pacific. Both PC1 and PC2 also have spectral power peaking near 70 and 50 days (Figure S1a in Supporting Information S1), consistent with the observed broadband

power of KWs (Kessler et al., 1995; Shinoda et al., 2008). Based on these results, we interpret the Equator only EOF1 and EOF2 as describing equatorially trapped intraseasonal KWs, consistent with Rydbeck et al. (2019).

As discussed in the previous section, CTWs entering the CCS can originate in the tropical ocean and/or be generated locally by wind variability associated with stochastic weather noise or atmospheric teleconnections emanating from the tropics. Therefore, even in a lagged sense, it is unlikely that the time variability described by the Equator only PCs is representative of the full scope of CTWs that impact the U.S. west coast. In an attempt to better sample the range of CTWs flavors that propagate through the CCS, we repeat the above EOF analysis for two additional domains, which include: (1) All along-path grid cells, from 150°E on the equator to the Gulf of Alaska (referred to as "Equator + Coast"), and (2) Only the coastal grid cells poleward of SA (referred to as "Coast only").

The first two Equator + Coast EOFs (Figure 4b) explain 22.3% and 21.9% of the SSH variability, respectively. These EOFs are very similar to the first two Equator only EOFs, but with SSH patterns that are shifted in the positive along-path direction, including a stronger projection along the Central American coastline (SA to GC-E). Additionally, the corresponding PCs show a similar lagged relationship between the Equator + Coast EOF1 and EOF2 (Figure 4d; orange line), with similar spectral peaks at 70 and 50 days (Figure S1b in Supporting Information S1). Taken together, we interpret the Equator + Coast EOFs as describing propagating intraseasonal KWs, but with a greater focus on those KWs that make the transition from the equator to the coast upon reaching South America. In particular, it is apparent from comparing Figures 4a and 4b that greater amplitude equatorial waves that favor the eastern side of the equatorial strip would tend to lead to larger amplitude coastal waves.

The first two Coast only EOFs explain 31.4% and 30.2% of the coastal SSH variability, respectively. These EOFs have a now familiar off-set dipolar structure, except the order of the EOF patterns is switched relative to the other two domains (e.g., Coast only EOF1 is analogous to the other domains' EOF2, and vice versa). Additionally, the Coast only EOF anomalies extend well into the CCS, with peak anomalies near the entrance to the Gulf of California and much weaker anomalies along the equatorial Pacific. The Coast only PC1 and PC2 have similar wave-like phase lags (Figure 4d; green line), but the peak correlations between the two PCs are found at shorter lags, suggesting a more rapidly propagating wave. The shorter timescale is reflected in the corresponding power spectra, which show a shift toward shorter periods due to a reduction in power at ~70 days (Figure S1c). These results suggest that the Coast only EOFs are describing the evolution of CTWs across dynamical origins, ranging from equatorially trapped KWs that continue along the coastline to locally generated CTWs (Enfield & Allen, 1983; Frischknecht et al., 2015).

3.3. Coastal Kelvin Wave Index

Kelvin wave indices can be derived from the information contained in each pair of normalized PCs. Specifically, the amplitude for a given KW index at time step t is defined as:

$$\text{Amplitude}(t) = \sqrt{PC1(t)^2 + PC2(t)^2} \quad (1)$$

In addition to the amplitude, the phase relationship between each pair of PCs can be computed to isolate the physical location of a wave at a given time step (see Supporting Information). Compositing filtered SSH anomalies on both phase and amplitude confirms that our EOFs capture waves that propagate in the positive along-path direction (Figure S2 in Supporting Information S1).

The amplitudes for the Equator only KW (E-KW) index, the Equator + Coast KW (EC-KW) index, and the Coast only KW (C-KW) index are shown in Figures 5a–5c. Peaks in the indices often occur during strong El Niño events (red shading), highlighting ENSO's role in driving intraseasonal KWs along the equator and up the North American coastline. There are also periods of elevated intensity in each of our indices that do not correspond with ENSO, which may be associated with the MJO or other sources of wind forcing in the western equatorial Pacific (Hendon et al., 1998; Kessler et al., 1995; Luther et al., 1983; Seiki & Takayabu, 2007; Zhang, 2001). Indeed, the E-KW, EC-KW, and C-KW indices are all phase lagged with the OLR-based MJO (OMI) index (Kiladis et al., 2014) with significant correlations of 0.34, 0.29, and 0.2 when the OMI leads by 12, 13, and 70 days, respectively (not shown).

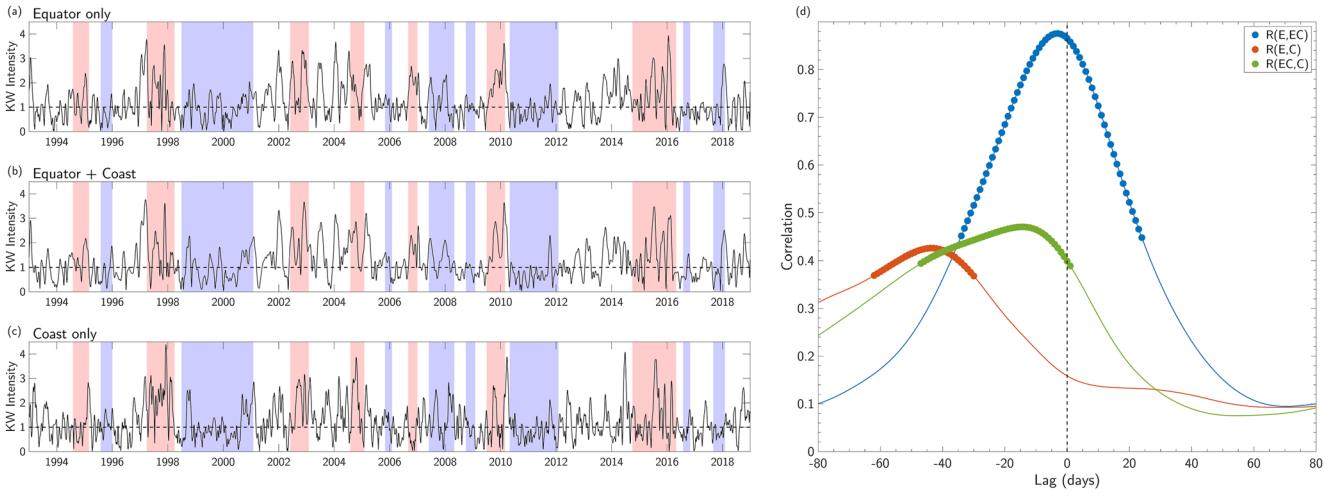

Figure 5. Amplitudes for the (a) Equator only KW (E-KW) index, (b) the Equator + Coast KW (EC-KW) index, and (c) the Coast only KW (C-KW) index. Red and blue shading indicate El Niño and La Niña periods, respectively. Dashed black lines mark the threshold used to determine robust Kelvin wave activity in each index. (d) Lag correlations between each combination of the E-KW index, the EC-KW index, and the C-KW index. The first index listed in each row of the legend leads at negative lags. For example, for lag correlations between the E-KW index and the EC-KW index (blue), the E-KW index leads at negative lags. Stippling denotes significant correlations at a 90% confidence interval.

The lagged relationships between our indices are consistent with our physical interpretation of the corresponding EOFs. For example, the peak correlation between the E-KW index and the EC-KW index is 0.88 and it occurs when the E-KW index leads by 3 days (Figure 5d, blue line). The high correlations near zero lag suggest the EC-KW index is primarily describing the same time variability of equatorially trapped KWs as the E-KW index, but the slightly higher correlations when the E-KW index leads reflects the additional lagged information of equatorial KWs transitioning onto the South American coastline captured by the EC-KW index.

Perhaps of more interest are the lag correlations of the E-KW and EC-KW indices with the C-KW index (Figure 5d, green and orange lines). The peak correlation between the E-KW index and the C-KW index is 0.43 when the E-KW index leads by 44 days, while the peak correlation between the EC-KW index and the C-KW index is 0.47 when the EC-KW index leads by 14 days. The significant correlations at long leads support our earlier conclusion that the C-KW index partially represents the time variability of coastally trapped KWs that originated along the equatorial Pacific. However, the comparatively lower maximum lag correlation between the equatorial indices and C-KW index further reinforces that the C-KW index is also capturing CTW variability that is locally forced and independent of tropical ocean waves. Therefore, of our three indices, the C-KW index is the most complete representation of the time variability of CTWs (regardless of dynamical origin), and may be thought of more broadly as a "CTW index." However, for simplicity and to be consistent with the notation of the other two indices, we will refer to it as the "C-KW index" in the remaining sections.

3.4. S2S Forecast Skill Assessment

In this section, we use our new C-KW index to assess whether CTWs provide an opportunity for enhanced S2S forecast skill in the CCS. To begin, we first evaluate the S2S ensemble mean forecast skill as a function of lead time and initialization day in the three CCS subregions (outlined Figure 1). In the South and Central CCS regions, the S2S model produces significant forecast skill (e.g., R^2 greater than 0 at the 90% confidence level) at nearly all initializations and all lead times (Figures 6a and 6b). While impressive, much of this skill is derived from damped persistence, as the SSH anomalies in these regions are highly autocorrelated within our 46 days forecasting window (Figure S3 in Supporting Information S1). Despite the strong day-to-day persistence, however, there are clusters of initialization days throughout the year in each region where the dynamical forecast is significantly more skillful than persistence at leads greater than ~15 days (red stippling). For example, the South CCS S2S forecasts show consistent dynamical skill above persistence at long leads when initializing in the summer and early fall. The Central CCS S2S forecasts significantly exceed persistence forecast skill primarily when initializing in summer. Further, the RMSE values in the South and Central CCS tend to be lowest (~2–3 cm) when the dynamical

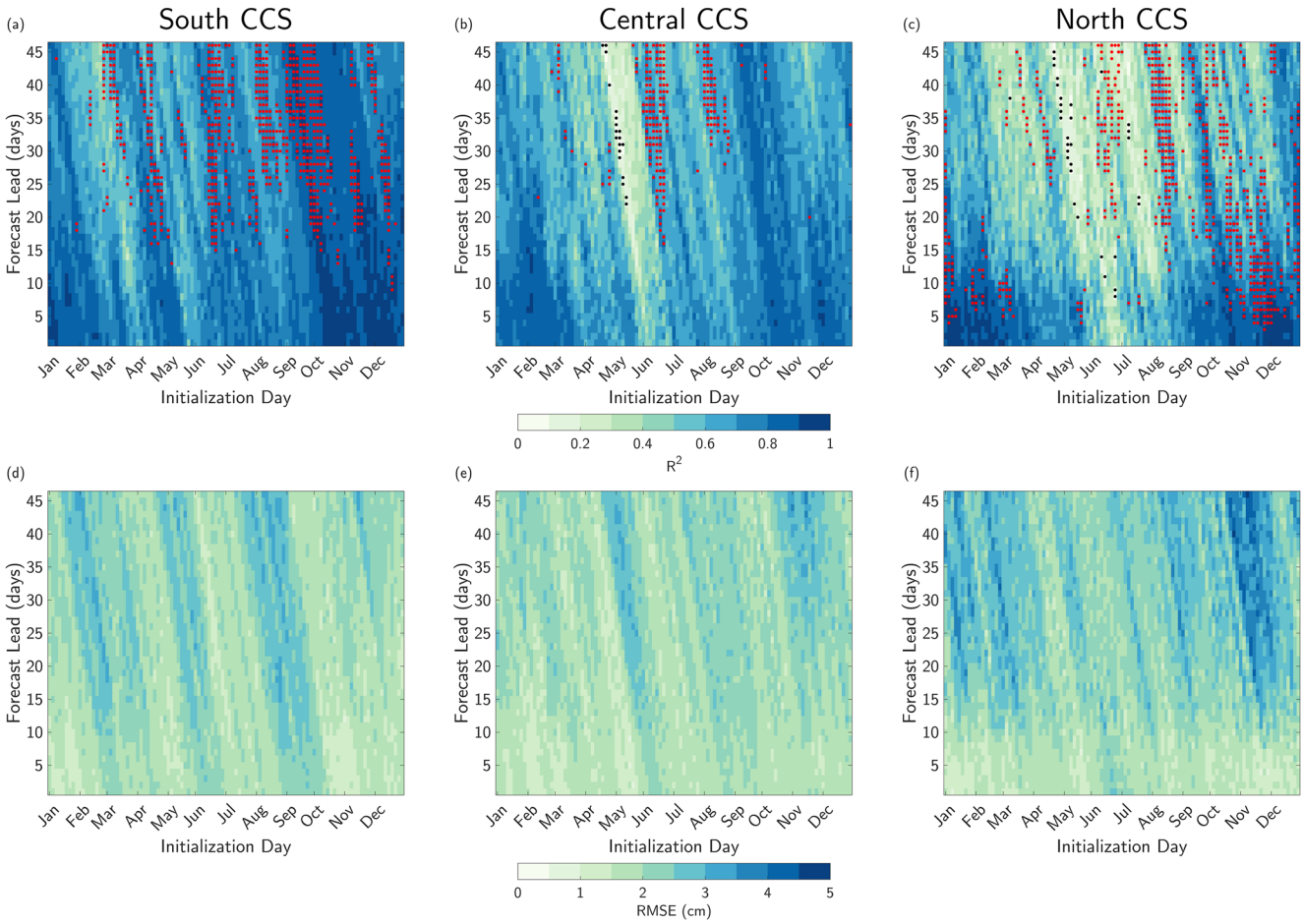

Figure 6. (a–c) Squared anomaly correlation coefficients (R^2; shading) between the S2S sea surface height (SSH) anomaly forecasts and GLORYS SSH anomalies as a function of forecast lead and initialization day. (d–f) As in (a–c), but for root-mean-square error (RMSE) (cm) between the S2S SSH anomaly forecast and the GLORYS SSH anomalies. Forecast skill is shown for (left column) the South California Current System (CCS), (middle column) the Central CCS, and (right column) North CCS. Forecast data for each region were computed by averaging together SSH anomalies at the coastal S2S grid cells within each domain (see Figure 1 colored boxes for regional boundaries). Black stippling in (a–c) indicates insignificant forecast skill. No stippling indicates forecast skill significantly greater than 0, but not significantly greater than that of a persistence forecast. Red stippling indicates forecast skill that is both significantly greater than 0 and significantly higher than that of the corresponding persistence forecast. All significance indicators are relative to a 90% confidence interval.

forecast is significantly more skillful than persistence (Figures 6d and 6e). This suggests that the dynamical forecasts are not only capturing the temporal evolution of SSH anomalies in these regions, but also their magnitude.

In comparison to the South and Central CCS regions, the North CCS S2S forecast skill is weaker overall and the RMSE values are larger, although the correlation values are still generally significantly above 0 (Figures 6c and 6f). Additionally, the North CCS forecast skill is more seasonally dependent, with the highest forecast skill at all leads occurring in the fall and winter and the lowest occurring in the spring and summer. Even though the forecast skill is generally weaker in the North CCS, the dynamical forecasts initialized in the late fall and winter show significant skill above persistence at shorter leads (5–20 days). In the summer, the dynamical forecasts are also significantly more skillful than persistence, but at leads greater than ~20 days.

The weaker overall forecast skill and the higher overall RMSE values in the North CCS region is likely due to increased weather noise at higher latitudes, which would impart stronger atmospheric forcing on the upper ocean and increase SSH variability along the coast. The increased SSH variance in the North CCS region is apparent when comparing the tide gauge data at northern latitudes (Figures 2a–2c) with those from southern latitudes (Figures 2g–2i). Increased variance also tends to decrease day-to-day persistence of SSH anomalies (as seen in the North CCS autocorrelation function; Figure S3 in Supporting Information S1), which would explain how the dynamical forecasts skill are significantly better than persistence at shorter leads for much of the year.

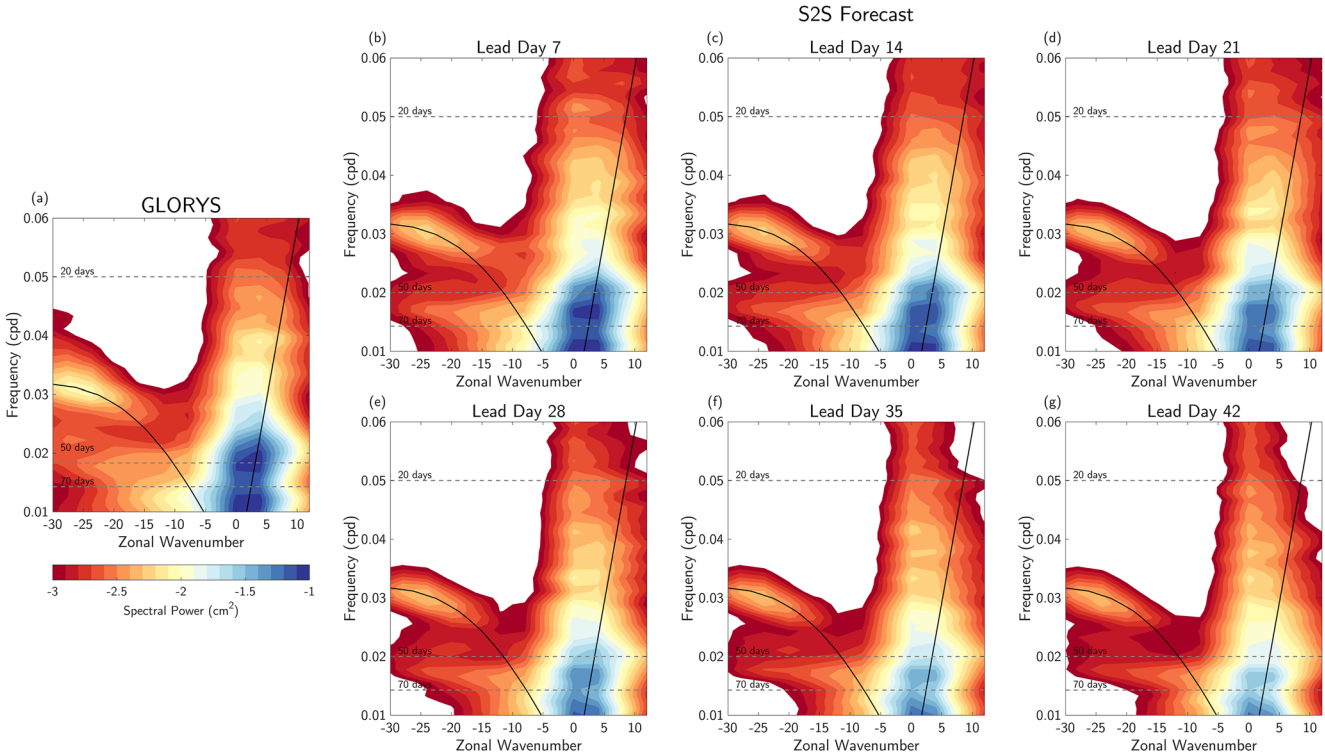

Figure 7. Wavenumber-frequency spectra of unfiltered sea surface height (SSH) anomalies averaged 2°S–2°N from 170°W to the South American coastline in (a) GLORYS and (b–g) the S2S forecast model at different lead times. Dashed gray lines mark periods of interest. Black lines at negative wavenumbers mark the dispersion relation for equatorial Rossby waves. Black lines at positive wavenumbers mark wave phase speeds of 2.7 m/s.

In order to further evaluate the S2S forecast skill in the context of propagating KWs, we assess the S2S model's ability to accurately simulate the physical evolution of these waves using wavenumber-frequency spectra. The GLORYS wavenumber-frequency spectrum shows two major features (Figure 7a). The first includes a spectral peak at negative (westward propagating) wavenumbers following the dispersion curve of equatorial Rossby waves. The second spectral peak occurs near wavenumbers 2–3 and periods of 50–70 days, which closely corresponds to first baroclinic KWs propagating eastward with a phase speed of ~2.7 m/s (Shinoda et al., 2008). Comparing to the S2S model spectra of forecasted SSH anomalies at increasing leads, we see a decrease in power of the major Rossby wave and KW spectral peaks as lead time increases (Figures 7b–7g). This reduction in power is likely due to the decrease in overall equatorial SSH variance seen in the S2S model at increased lead times (Figure S4 in Supporting Information S1). However, the presence and consistency of the two spectral peaks at long leads suggests the S2S model is credibly simulating equatorial wave dynamics over the duration of the forecasts.

Finally, we stratify the S2S ensemble mean forecast skill in each of the CCS subregions based on the intensity of our C-KW index at forecast initialization (Figure 8). Doing so will allow us to determine if CTWs provide an opportunity for enhanced forecast skill. We first compute weekly averages of the S2S ensemble mean forecasts and the resampled GLORYS data. Each week represents a 7-day average (i.e., week 1 corresponds to the average forecast at days 1–7), except for week 7, which is the average forecast at days 43–46. We then calculate the lead-dependent R^2 of the weekly averaged forecasts that fall within three C-KW index intensity categories—Weak, Strong, or Extreme—at initialization. These intensity categories are defined as terciles based on the distribution of all C-KW index values that fall on a forecast initialization day and are also above 1. The lower bounds of the terciles are 1.33 and 1.84. For example, a forecast falls within the "Weak" KW category if it is initialized with a C-KW index value between 1 and 1.33. The Weak, Strong, and Extreme KW categories have sample sizes of 348, 348, and 358, respectively. They are then comparable to initializations with no significant KW activity (i.e., C-KW index values below 1), which has a sample size of 928.

Focusing first on all initialization days (i.e., regardless of C-KW index intensity, N = 1,982), the persistence forecasts (Figure 8; dashed black lines) in each CCS subregion have higher skill than the dynamical forecasts

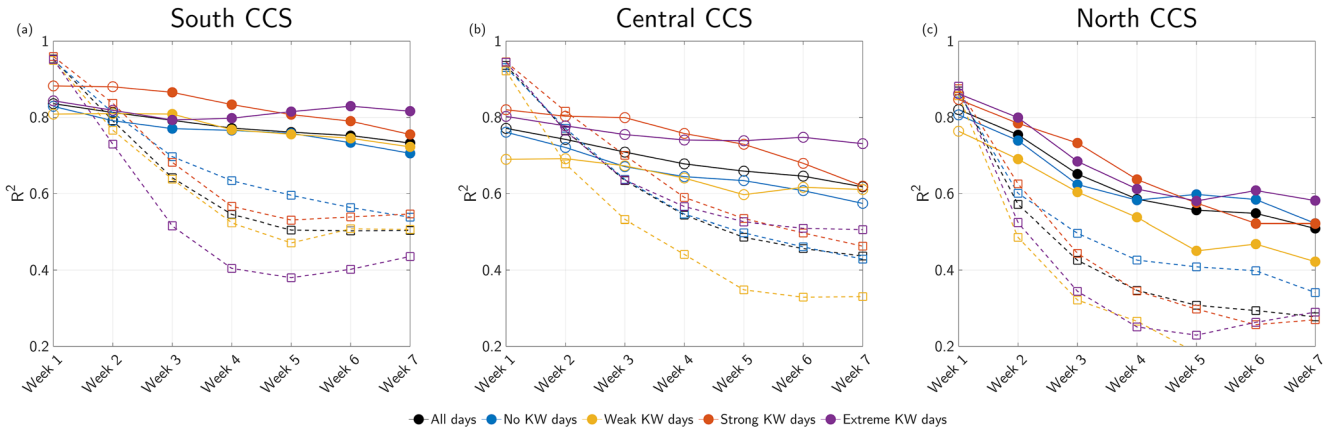

Figure 8. Forecast skill as a function of lead time and Kelvin waves (KW) intensity at initialization in (a) the South California Current System (CCS), (b) the Central CCS, and (c) the North CCS. Forecast data for each region were computed by averaging together SSH anomalies at the coastal S2S grid cells within each domain (see Figure 1 colored boxes for regional boundaries). Forecast skill across all initializations (i.e., "All days") is in black. Forecast skill for forecasts initialized during No, Weak, Strong, and Extreme Kelvin wave conditions are in blue, yellow, orange, and purple, respectively. All dynamical forecast skill scores (solid lines) are significantly greater than 0. Filled circles mark lead times where the dynamical forecasts have significant skill above persistence (squares, dashed lines). All significance indicators are relative to a 90% confidence interval.

(solid black lines) at short lead times (~1–2 weeks). This is consistent with Figure 6, and may be expected given the slow decay of the SSH autocorrelation function at lags of only a couple weeks. At longer leads, however, the dynamical forecasts in the South and North CCS show enhanced predictability. In the South CCS, the all-days dynamical forecast skill is significantly higher than the all-days persistence skill in weeks 3–7, explaining over 20% more of the SSH variance at these leads. In the North CCS, the forecast skill is lower overall, but the all-days persistence forecast skill rapidly declines from weeks 1–3 due to the stronger weather-related SSH variability at these latitudes. As a result, the all-days dynamical forecasts become significantly more skillful than persistence in weeks 2–7, also explaining over 20% more of the SSH variance at these leads.

How does coastal KW (or more broadly CTW) intensity at initialization impact dynamical forecast skill in each region? When initializing with Strong KW conditions in the South CCS (Figure 8a; orange lines), the dynamical forecast skill is significantly higher than persistence at weeks 3–7, as well as higher than the all-days dynamical forecast skill at all leads. Dynamical forecast skill is further enhanced in the South CCS at weeks 5–7 when initializing with Extreme KW conditions (Figure 8a; purple lines), explaining over 40% more SSH variance than the Extreme KW persistence forecast and over 10% more SSH variance than dynamical forecasts initialized without significant KW activity (e.g., No KW days; blue lines) in week 7. Initializing forecasts during Weak KW days (Figure 8a; yellow lines) does not appreciably impact the forecast skill in this region.

In the Central CCS, accounting for KW intensity at initialization yields similar dynamical forecast skill enhancements as those seen in the South CCS (Figure 8b). However, none of the dynamical forecasts are significantly more skillful than persistence at the 90% confidence level. In the North CCS, dynamical forecasts initialized on Strong KW days have higher skill than the all-days dynamical forecasts at weeks 1–5 (Figure 8c). Similarly, initializing on Extreme KW days produces week 7 dynamical forecasts that explain 30% more SSH variability than the persistence forecast and 6% more SSH variability than the dynamical forecasts initialized on No KW days. The presence of Weak KW conditions at initialization lowers the dynamical forecast skill at all leads (even relative to No KW days), but these forecasts are still significantly more skillful than the corresponding persistence forecasts from weeks 2–7. Taken together, the results shown in Figure 8 suggest that the presence of coastal KW activity at initialization generally enhances dynamical forecast skill of CCS SSH anomalies, particularly at longer leads (weeks 4–7) and for more intense KWs.

3.5. Real-Time C-KW Index

In order to assist future operational efforts that may want to utilize the C-KW index in real time, we follow previous studies (Kikuchi et al., 2012; Kiladis et al., 2014; Rydbeck et al., 2019) in obtaining an approximation of the C-KW index based on real-time SSH anomalies. These steps are necessary because the actual C-KW index

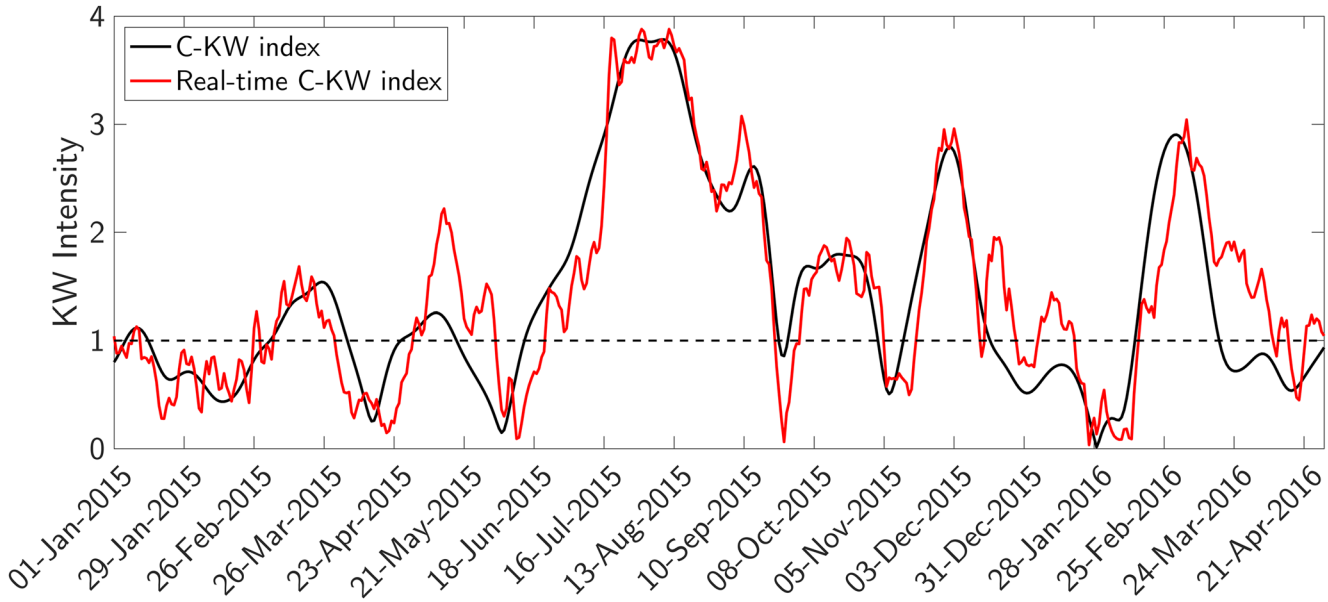

Figure 9. The actual Coast only KW (C-KW) index (black) compared to the approximated real-time C-KW index (red) for an active coastal Kelvin wave period.

(Figure 5c) is based on bandpass filtered SSH anomalies, which requires forward temporal filtering and is not possible in real time.

Following the Rydbeck et al. (2019), we formulate a real-time C-KW index by first removing the first three harmonics of the seasonal cycle from the coastal along-path GLORYS SSH anomalies (i.e., from SA to the Gulf of Alaska). We then apply a wavenumber filter which retains only positive wavenumbers (i.e., waves propagating with the coast located to the right of propagation vector). To remove low-frequency variability at each grid point, we then subtract the mean of the previous 55 days from each time step of interest. Our results are insensitive to minor changes in the number of days averaged.

The resulting SSH anomalies are then projected on our Coast only EOF1 and EOF2 patterns at each time step, producing real-time estimates of the Coast only PC1 and PC2. Finally, we use Equation 1 to formulate the real-time C-KW index. Over the period 1993–2018, the actual C-KW index and the real-time C-KW index are highly correlated with a value of 0.87. Figure 9 shows that the two indices are very highly correlated during the active 2015–2016 CTW period discussed in Figure 3. The high overall correlation and the close correspondence between the different indices during this active KW period suggests that the real-time C-KW index may be useful for real-time forecasting applications.

4. Summary and Conclusions

In this study, we conducted the first S2S forecast skill assessment of SSH anomalies in the CCS. We found that dynamical forecasts initialized every 3–4 days from 2000-2018 by the ECMWF S2S forecasting model skillfully predict observed SSH anomalies throughout the coastal CCS (Figure 6). In particular, the S2S model reforecasts have significant skill above persistence in the South CCS at lead times greater than ∼15 days in the summer and fall. In the North CCS, dynamical forecast skill was significantly above persistence beginning at shorter leads in the winter (∼day 5) and at longer leads in the summer (∼day 20), which was primarily due to the weaker day-to-day persistence of SSH anomalies at these latitudes. Dynamical forecasts in the Central CCS were also skillful, but rarely more so than the persistence forecast.

In addition, we showed that dynamical forecast skill is enhanced when robust coastal KW activity is present at forecast initialization (Figure 8). This enhanced skill was particularly apparent in the South CCS and North CCS at long leads (e.g., week 4-week 7), where forecasts initialized during Strong or Extreme KW conditions explained a remarkable 30–40% more observed SSH variability than the corresponding persistence forecasts and 6–10% more SSH variability than the dynamical forecasts initialized without significant KW activity. To

characterize CTW variability in the forecasts, we built on previous studies (e.g., Rydbeck et al., 2019) to develop a new coastal KW (C-KW) index (Figure 5c) based on EOFs of coastal SSH anomalies in a high-resolution ocean reanalysis. The amplitude and phase information contained in our C-KW index describes the propagation of intraseasonal CTWs from a variety of dynamical origins, ranging from equatorially trapped KWs continuing up the Central and North American coastlines to waves generated by local wind effects. Finally, in support of operational forecasting efforts, we showed that our C-KW index can be reliably estimated in real time.

Our results have a number of implications for the broader marine research community and for potential developments in managing marine resources and coastal infrastructure. First, the ECMWF S2S model consistently produces dynamically skillful SSH forecasts along the U.S. west coast, and can be considered as a decision support tool for applications where coastal SSH is a key variable. As more modeling centers begin offering S2S forecasts of ocean variables, it will be important to further assess regional forecast skill across a range of model configurations. We call on other S2S modeling participants to consider prioritizing SSH (and other ocean variables) as a publicly available output of future forecasts. Second, our work highlights GLORYS as a powerful tool for studying the detailed evolution of the coastal ocean in the recent observational record. In particular, the dynamical insights provided by our new C-KW index combined with the high spatial resolution of GLORYS present an opportunity to retrospectively study the relationship between observed coastal KW activity and measured impacts on CCS marine ecosystems with fresh perspective.

Additionally, the physical evolution of CTWs through the CCS provides an important forecast opportunity for enhanced prediction skill of coastal SSH, particularly at lead times of 4–7 weeks. These results may aid in decisions for adapting coastal infrastructure to increased flood risk in the face of continued mean sea level rise (Jacox et al., 2020; Widlansky et al., 2017; Woodworth et al., 2019), as well as other applications for which SSH is linked to broader ecosystem change (e.g., upwelling, species distributions). To further examine the potential for this type of decision support, we intend to follow-up this study by assessing the physical relationship between coastal SSH variability and subsequent changes to marine ecosystem-relevant variables such as SST, bottom temperature, mixed layer depth, upwelling, and horizontal currents. Such an analysis would provide marine stakeholders with improved understanding of how regional sea level changes map on to ecosystem and infrastructure impacts, and thus how best to utilize S2S forecasts for decision making.

Finally, while our focus was primarily on coastal KW variability, we echo previous studies (e.g., Stan et al., 2017) emphasizing the broader importance of deterministic climate processes as sources of enhanced forecast skill. In particular, climate processes that are well understood physically (such as the propagation of a coastal KW) may be more accurately simulated by models, and thus contribute to a more reliable forecast when they are captured in a forecast initialization. Therefore, it is possible that other rapidly evolving oceanic or atmospheric teleconnections related to climate modes (e.g., ENSO) or organized convection (e.g., the MJO) may provide additional forecast opportunities for the U.S. coastal ocean on S2S timescales.

Data Availability Statement

The GLORYS reanalysis data used in this study are freely available at: https://resources.marine.copernicus.eu/products. The ECMWF S2S reforecasts can be found at: https://confluence.ecmwf.int/display/S2S.

Acknowledgments
We thank George Kiladis and Brandon Wolding for their helpful comments over the course of this study. We further thank Yan Wang for her assistance in downloading and processing the ECMWF forecasts analyzed in this study. We also thank two anonymous reviewers for their insightful comments and suggestions that improved the quality of this work. D. J. A. was funded by a Postdoctoral Fellowship with the Cooperative Institute for Research in Environmental Sciences (CIRES) at the University of Colorado Boulder and by a grant funded by the NOAA Climate Program Office's Modeling, Analysis, Predictions, and Projections Program and the NOAA Fisheries Office of Science and Technology.

References

Amaya, D. J., Bond, N. E., Miller, A. J., & Deflorio, M. J. (2016). The evolution and known atmospheric forcing mechanisms behind the 2013–2015 North Pacific warm anomalies. *US CLIVAR Variations*, *14*(2), 1–6.

Batstone, C., & Hendon, H. H. (2005). Characteristics of stochastic variability associated with ENSO and the role of the MJO. *Journal of Climate*, *18*(11), 1773–1789. https://doi.org/10.1175/JCLI3374.1

Bergman, J. W., Hendon, H. H., & Weickmann, K. M. (2001). Intraseasonal air-sea interaction at the onset of El Niño. *Journal of Climate*, *14*(8), 1702–1719. https://doi.org/10.1175/1520-0442(2001)014<1702:IASIAT>2.0.CO;2

Bond, N. A., Cronin, M. F., Freeland, H., & Mantua, N. (2015). Causes and impacts of the 2014 warm anomaly in the NE Pacific. *Geophysical Research Letters*, *42*, 3414–3420. https://doi.org/10.1002/2015GL063306

Busalacchi, A. J., Takeuchi, K., & O'Brien, J. J. (1983). Interannual variability of the equatorial Pacific-revisited. *Journal of Geophysical Research*, *88*(C12), 7551–7562. https://doi.org/10.1029/JC088iC12p07551

Capotondi, A., Sardeshmukh, P. D., Di Lorenzo, E., Subramanian, A. C., & Miller, A. J. (2019). Predictability of US west coast ocean temperatures is not solely due to ENSO. *Scientific Reports*, *9*(1), 10993. https://doi.org/10.1038/s41598-019-47400-4

Checkley, D. M., & Barth, J. A. (2009). Patterns and processes in the California current system. *Progress in Oceanography*, *83*(1–4), 49–64. https://doi.org/10.1016/j.pocean.2009.07.028

Cravatte, S., Picaut, J., & Eldin, G. (2003). Second and first baroclinic Kelvin modes in the equatorial Pacific at intraseasonal timescales. *Journal of Geophysical Research*, *108*(8), 3266. https://doi.org/10.1029/2002JC001511

DeMott, C., Muñoz, Á. G., Roberts, C. D., Spillman, C. M., & Vitart, F. (2021). The benefits of better ocean weather forecasting. *Eos*, *102*. https://doi.org/10.1029/2021EO210601

Ding, H., Alexander, M. A., & Jacox, M. G. (2021). Role of geostrophic currents in future changes of coastal upwelling in the California current system. *Geophysical Research Letters*, *48*, e2020GL090768. https://doi.org/10.1029/2020GL090768

Dorman, C. E., & Winanat, C. D. (1995). Buoy observations of the atmosphere along the west coast of the United States, 1981–1990. *Journal of Geophysical Research*, *100*(C8), 16029–16044. https://doi.org/10.1029/95JC00964

Enfield, D. B., & Allen, J. S. (1980). On the structure and dynamics of monthly mean sea level anomalies along the Pacific coast of north and South America. *Journal of Physical Oceanography*, *10*(4), 557–578. https://doi.org/10.1175/1520-0485(1980)010<0557:OTSADO>2.0.CO;2

Enfield, D. B., & Allen, J. S. (1983). The generation and propagation of sea level variability along the Pacific coast of Mexico. *Journal of Physical Oceanography*, *13*(6), 1012–1033. https://doi.org/10.1175/1520-0485(1983)013<1012:TGAPOS>2.0.CO;2

Enfield, D. B., Cornejo-Rodriguez, M. D. P., Smith, R. L., & Newberger, P. A. (1987). The equatorial source of propagating variability along the Peru coast during the 1982–1983 El Niño. *Journal of Geophysical Research*, *92*, 14335–14346. https://doi.org/10.1029/JC092iC13p14335

Eriksen, C. C., Blumenthal, M. B., Hayes, S. P., & Ripa, P. (1983). Wind-generated equatorial Kelvin waves observed across the Pacific Ocean. *Journal of Physical Oceanography*, *13*(9), 1622–1640. https://doi.org/10.1175/1520-0485(1983)013<1622:WGEKWO>2.0.CO;2

Fisher, R. A. (1915). Frequency distribution of the values of the correlation coefficient in samples from an indefinitely large population. *Biometrika*, *10*(4), 507–521. https://doi.org/10.2307/2331838

Fisher, R. A. A. (1924). The distribution of the partial correlation coefficient. *Metron*, *3*, 329–332.

Frischknecht, M., Münnich, M., & Gruber, N. (2015). Remote versus local influence of ENSO on the California current system. *Journal of Geophysical Research: Oceans*, *120*, 1353–1374. https://doi.org/10.1002/2014JC010531

Goddard, L., Mason, S. J., Zebiak, S. E., Ropelewski, C. F., Basher, R., & Cane, M. A. (2001). Current approaches to seasonal-to-interannual climate predictions. *International Journal of Climatology*, *21*(9), 1111–1152. https://doi.org/10.1002/joc.636

Gómez-Valdivia, F., Parés-Sierra, A., & Laura Flores-Morales, A. (2017). Semiannual variability of the California undercurrent along the southern California current system: A tropical generated phenomenon. *Journal of Geophysical Research: Oceans*, *122*, 1574–1589. https://doi.org/10.1002/2016JC012350

Hazen, E. L., Palacios, D. M., Forney, K. A., Howell, E. A., Becker, E., Hoover, A. L., et al. (2017). WhaleWatch: A dynamic management tool for predicting blue whale density in the California current. *Journal of Applied Ecology*, *54*(5), 1415–1428. https://doi.org/10.1111/1365-2664.12820

Hazen, E. L., Scales, K. L., Maxwell, S. M., Briscoe, D. K., Welch, H., Bograd, S. J., et al. (2018). A dynamic ocean management tool to reduce bycatch and support sustainable fisheries. *Science Advances*, *4*(5), eaar3001. https://doi.org/10.1126/sciadv.aar3001

Hendon, H. H., Liebmann, B., & Glick, J. D. (1998). Oceanic Kelvin waves and the Madden-Julian oscillation. *Journal of the Atmospheric Sciences*, *55*(1), 88–101. https://doi.org/10.1175/1520-0469(1998)055<0088:OKWATM>2.0.CO;2

Hervieux, G., Alexander, M. A., Stock, C. A., Jacox, M. G., Pegion, K., Becker, E., et al. (2019). More reliable coastal SST forecasts from the North American multimodel ensemble. *Climate Dynamics*, *53*, 7153–7168. https://doi.org/10.1007/s00382-017-3652-7

Hobday, A. J., Spillman, C. M., Eveson, J. P., Hartog, J. R., Zhang, X., & Brodie, S. (2018). A framework for combining seasonal forecasts and climate projections to aid risk management for fisheries and aquaculture. *Frontiers in Marine Science*, *5*, 137. https://doi.org/10.3389/fmars.2018.00137

Howell, E. A., Kobayashi, D. R., Parker, D. M., Balazs, G. H., & Polovina, J. J. (2008). TurtleWatch: A tool to aid in the bycatch reduction of loggerhead turtles *Caretta caretta* in the Hawaii-based pelagic longline fishery. *Endangered Species Research*, *5*(2–3), 267–278. https://doi.org/10.3354/esr00096

Hughes, C. W., Fukumori, I., Griffies, S. M., Huthnance, J. M., Minobe, S., Spence, P., et al. (2019). Sea level and the role of coastal trapped waves in mediating the influence of the open ocean on the coast. *Surveys in Geophysics*, *40*, 1467–1492. https://doi.org/10.1007/s10712-019-09535-x

Jacox, M. G., Alexander, M. A., Siedlecki, S., Chen, K., Kwon, Y. O., Brodie, S., et al. (2020). Seasonal-to-interannual prediction of North American coastal marine ecosystems: Forecast methods, mechanisms of predictability, and priority developments. *Progress in Oceanography*, *183*, 102307. https://doi.org/10.1016/j.pocean.2020.102307

Jacox, M. G., Alexander, M. A., Stock, C. A., & Hervieux, G. (2019). On the skill of seasonal sea surface temperature forecasts in the California Current System and its connection to ENSO variability. *Climate Dynamics*, *53*(12), 7519–7533. https://doi.org/10.1007/s00382-017-3608-y

Jacox, M. G., Edwards, C. A., Hazen, E. L., & Bograd, S. J. (2018). Coastal upwelling revisited: Ekman, Bakun, and improved upwelling indices for the U.S. West coast. *Journal of Geophysical Research: Oceans*, *123*, 7332–7350. https://doi.org/10.1029/2018JC014187

Jacox, M. G., Fiechter, J., Moore, A. M., & Edwards, C. A. (2015). ENSO and the California current coastal upwelling response. *Journal of Geophysical Research: Oceans*, *120*, 1691–1702. https://doi.org/10.1002/2014JC010650

Jacox, M. G., Hazen, E. L., Zaba, K. D., Rudnick, D. L., Edwards, C. A., Moore, A. M., & Bograd, S. J. (2016). Impacts of the 2015–2016 El Niño on the California current system: Early assessment and comparison to past events. *Geophysical Research Letters*, *43*, 7072–7080. https://doi.org/10.1002/2016GL069716

Johnson, M. A., & O'Brien, J. J. (1990). The role of coastal Kelvin waves on the northeast Pacific Ocean. *Journal of Marine Systems*, *1*(1–2), 29–38. https://doi.org/10.1016/0924-7963(90)90085-O

Karnauskas, K. B. (2013). Can we distinguish canonical El Niño from Modoki? *Geophysical Research Letters*, *40*, 5246–5251. https://doi.org/10.1002/grl.51007

Kessler, W. S., & Kleeman, R. (2000). Rectification of the Madden-Julian oscillation into the ENSO cycle. *Journal of Climate*, *13*(20), 3560–3575. https://doi.org/10.1175/1520-0442(2000)013<3560:ROTMJO>2.0.CO;2

Kessler, W. S., & McPhaden, M. J. (1995). The 1991–1993 El Niño in the central Pacific. *Deep-Sea Research Part II*, *42*(2–3), 295–333. https://doi.org/10.1016/0967-0645(95)00041-N

Kessler, W. S., McPhaden, M. J., & Weickmann, K. M. (1995). Forcing of intraseasonal Kelvin waves in the equatorial Pacific. *Journal of Geophysical Research*, *100*(C6), 10613–10631. https://doi.org/10.1029/95JC00382

Kikuchi, K., Wang, B., & Kajikawa, Y. (2012). Bimodal representation of the tropical intraseasonal oscillation. *Climate Dynamics*, *38*(9–10), 1989–2000. https://doi.org/10.1007/s00382-011-1159-1

Kiladis, G. N., Dias, J., Straub, K. H., Wheeler, M. C., Tulich, S. N., Kikuchi, K., et al. (2014). A comparison of OLR and circulation-based indices for tracking the MJO. *Monthly Weather Review*, *142*(5), 1697–1715. https://doi.org/10.1175/MWR-D-13-00301.1

Kirtman, B. P., Min, D., Infanti, J. M., Kinter, J. L., Paolino, D. A., Zhang, Q., et al. (2014). The North American multimodel ensemble: Phase-1 seasonal-to-interannual prediction; phase-2 toward developing intraseasonal prediction. *Bulletin of the American Meteorological Society*, *95*(4), 585–601. https://doi.org/10.1175/BAMS-D-12-00050.1

Kutsuwada, K., & McPhaden, M. (2002). Intraseasonal variations in the upper equatorial Pacific Ocean prior to and during the 1997-98 El Niño. *Journal of Physical Oceanography*, *32*(4), 1133–1149. https://doi.org/10.1175/1520-0485(2002)032<1133:IVITUE>2.0.CO;2

Lellouche, J.-M., Greiner, E., Bourdallé-Badie, R., Garric, G., Mellet, A., Drévillion, M., et al. (2021). The Copernicus global 1/12° oceanic and sea ice GLORYS12 reanalysis. *Frontiers of Earth Science*, *9*, 698876. https://doi.org/10.3389/feart.2021.698876

Lund, R. B., von Storch, H., & Zwiers, F. W. (2000). Statistical analysis in climate research. *Journal of the American Statistical Association*, *95*(452), 1375. https://doi.org/10.2307/2669798

Luther, D. S., Harrison, D. E., & Knox, R. A. (1983). Zonal winds in the central equatorial Pacific and El Niño. *Science*, *222*(4621), 327–330. https://doi.org/10.1126/science.222.4621.327

Lyman, J. M., & Johnson, G. C. (2008). Equatorial Kelvin wave influences may reach the Bering Sea during 2002 to 2005. *Geophysical Research Letters*, *35*, L14607. https://doi.org/10.1029/2008GL034761

McPhaden, M. J. (1999). Genesis and evolution of the 1997–98 El Nino. *Science*, *283*, 950–954. https://doi.org/10.1126/science.283.5404.950

McPhaden, M. J., Bahr, F., Du Penhoat, Y., Firing, E., Hayes, S. P., Niiler, P. P., et al. (1992). The response of the western equatorial Pacific Ocean to westerly wind bursts during November 1989 to January 1990. *Journal of Geophysical Research*, *97*(C9), 14289–14303. https://doi.org/10.1029/92JC01197

McPhaden, M. J., Freitag, H. P., Hayes, S. P., Taft, B. A., Chen, Z., & Wyrtki, K. (1988). The response of the equatorial Pacific Ocean to a westerly wind burst in May 1986. *Journal of Geophysical Research*, *93*(C9), 10589–10603. https://doi.org/10.1029/JC093ic09p10589

McPhaden, M. J., & Yu, X. (1999). Equatorial waves and the 1997–98 El Nino. *Geophysical Research Letters*, *26*(19), 2961–2964. https://doi.org/10.1029/1999GL004901

Mosquera-Vásquez, K., Dewitte, B., & Illig, S. (2014). The central Pacific El Niño intraseasonal Kelvin wave. *Journal of Geophysical Research: Oceans*, *119*, 6605–6621. https://doi.org/10.1002/2014JC010044

Nichols, C. R., Wright, L. D., Bainbridge, S. J., Cosby, A., Hénaff, A., Loftis, J. D., et al. (2019). Collaborative science to enhance coastal resilience and adaptation. *Frontiers in Marine Science*, *6*, 404. https://doi.org/10.3389/fmars.2019.00404

Roundy, P. E., & Kiladis, G. N. (2007). Analysis of a reconstructed oceanic Kelvin wave dynamic height dataset for the period 1974–2005. *Journal of Climate*, *20*(17), 4341–4355. https://doi.org/10.1175/JCLI4249.1

Rydbeck, A. V., Jensen, T. G., & Flatau, M. (2019). Characterization of intraseasonal Kelvin waves in the equatorial Pacific Ocean. *Journal of Geophysical Research: Oceans*, *124*, 2028–2053. https://doi.org/10.1029/2018JC014838

Seiki, A., & Takayabu, Y. N. (2007). Westerly wind burst and their relationship with intraseasonal variations and ENSO. Part II: Energetics over the western and central Pacific. *Monthly Weather Review*, *135*(10), 3346–3361. https://doi.org/10.1175/MWR3503.1

Seo, K. H., & Son, S. W. (2012). The global atmospheric circulation response to tropical diabatic heating associated with the Madden-Julian oscillation during northern winter. *Journal of the Atmospheric Sciences*, *69*(1), 79–96. https://doi.org/10.1175/2011JAS3686.1

Seo, K. H., & Xue, Y. (2005). MJO-related oceanic Kelvin waves and the ENSO cycle: A study with the NCEP global Ocean data assimilation system. *Geophysical Research Letters*, *32*, L07712. https://doi.org/10.1029/2005GL022511

Shin, S. I., & Newman, M. (2021). Seasonal predictability of global and north American coastal sea surface temperature and height anomalies. *Geophysical Research Letters*, *48*, e2020GL091886. https://doi.org/10.1029/2020GL091886

Shinoda, T., Roundy, P. E., & Kiladis, G. N. (2008). Variability of intraseasonal Kelvin waves in the equatorial Pacific Ocean. *Journal of Physical Oceanography*, *38*(5), 921–944. https://doi.org/10.1175/2007JPO3815.1

Siedlecki, S. A., Kaplan, I. C., Hermann, A. J., Nguyen, T. T., Bond, N. A., Newton, J. A., et al. (2016). Experiments with seasonal forecasts of ocean conditions for the Northern region of the California Current upwelling system. *Scientific Reports*, *6*, 27203. https://doi.org/10.1038/srep27203

Simmons, A. J., Wallace, J. M., & Branstator, G. W. (1983). Barotropic wave propagation and instability, and atmospheric teleconnection patterns. *Journal of the Atmospheric Sciences*, *40*(6), 1363–1392. https://doi.org/10.1175/1520-0469(1983)040<1363:BWPAIA>2.0.CO;2

Stan, C., Straus, D. M., Frederiksen, J. S., Lin, H., Maloney, E. D., & Schumacher, C. (2017). Review of tropical-extratropical teleconnections on intraseasonal time scales. *Reviews of Geophysics*, *55*, 902–937. https://doi.org/10.1002/2016RG000538

Stock, C. A., Pegion, K., Vecchi, G. A., Alexander, M. A., Tommasi, D., Bond, N. A., et al. (2015). Seasonal sea surface temperature anomaly prediction for coastal ecosystems. *Progress in Oceanography*, *137*, 219–236. https://doi.org/10.1016/j.pocean.2015.06.007

Strub, P. T., & James, C. (2002). The 1997–1998 oceanic El Niño signal along the southeast and northeast Pacific boundaries—An altimetric view. *Progress in Oceanography*, *54*, 439–458. https://doi.org/10.1016/S0079-6611(02)00063-0

Szekely, T., Gourrion, J., Pouliquen, S., & Reverdin, G. (2019). The CORA 5.2 dataset: Global in-situ temperature and salinity measurements dataset. Data description and validation. *Ocean Science Discussions*, 1–20. https://doi.org/10.5194/os-2018-144

Thorne, L. H., Baird, R. W., Webster, D. L., Stepanuk, J. E., & Read, A. J. (2019). Predicting fisheries bycatch: A case study and field test for pilot whales in a pelagic longline fishery. *Diversity and Distributions*, *25*(6), 909–923. https://doi.org/10.1111/ddi.12912

Tommasi, D., Stock, C. A., Hobday, A. J., Methot, R., Kaplan, I. C., Eveson, J. P., et al. (2017). Managing living marine resources in a dynamic environment: The role of seasonal to decadal climate forecasts. *Progress in Oceanography*, *152*, 15–49. https://doi.org/10.1016/j.pocean.2016.12.011

Vignudelli, S., Birol, F., Benveniste, J., Fu, L. L., Picot, N., Raynal, M., & Roinard, H. (2019). Satellite altimetry measurements of sea level in the coastal zone. *Surveys in Geophysics*, *40*, 1319–1349. https://doi.org/10.1007/s10712-019-09569-1

Vitart, F., Ardilouze, C., Bonet, A., Brookshaw, A., Chen, M., Codorean, C., et al. (2017). The subseasonal to seasonal (S2S) prediction project database. *Bulletin of the American Meteorological Society*, *98*(1), 163–173. https://doi.org/10.1175/BAMS-D-16-0017.1

Vitart, F., & Robertson, A. W. (2018). The sub-seasonal to seasonal prediction project (S2S) and the prediction of extreme events. *Npj Climate and Atmospheric Science*, *1*(1), 3.

Wallace, J. M., & Gutzler, D. S. (1981). Teleconnections in the geopotential height field during the Northern Hemisphere winter. *Monthly Weather Review*, *109*(4), 784–812. https://doi.org/10.1175/1520-0493(1981)109<0784:TITGHF>2.0.CO;2

Wang, D. P., & Mooers, C. N. K. (1976). Coastal-trapped waves in a continuously stratified ocean. *Journal of Physical Oceanography*, *6*(6), 853–863. https://doi.org/10.1175/1520-0485(1976)006<0853:CTWIAC>2.0.CO;2

Welch, H., Hazen, E. L., Bograd, S. J., Jacox, M. G., Brodie, S., Robinson, D., et al. (2019). Practical considerations for operationalizing dynamic management tools. *Journal of Applied Ecology*, *56*(2), 459–469. https://doi.org/10.1111/1365-2664.13281

Widlansky, M. J., Marra, J. J., Chowdhury, M. R., Stephens, S. A., Miles, E. R., Fauchereau, N., et al. (2017). Multimodel ensemble sea level forecasts for tropical Pacific Islands. *Journal of Applied Meteorology and Climatology*, *56*(4), 849–862. https://doi.org/10.1175/JAMC-D-16-0284.1

Woodworth, P. L., Melet, A., Marcos, M., Ray, R. D., Wöppelmann, G., Sasaki, Y. N., et al. (2019). Forcing factors affecting sea level changes at the coast. *Surveys in Geophysics*, *40*, 1351–1397. https://doi.org/10.1007/s10712-019-09531-1

Zhang, C. (2001). Intraseasonal perturbations in sea surface temperatures of the equatorial eastern Pacific and their association with the Madden-Julian oscillation. *Journal of Climate*, *14*(6), 1309–1322. https://doi.org/10.1175/1520-0442(2001)014<1309:IPISST>2.0.CO;2